Accepted manuscript. Link to final publication:
https://doi.org/10.1016/j.matchemphys.2018.10.049

©2019. This manuscript version is made available under the CC-BY-NC-ND 4.0 license http://creativecommons.org/licenses/by-nc-nd/4.0/

The Effect of Preparation Conditions on Magnetite Nanoparticles Obtained via Chemical Co-precipitation

Zoltán Klencsár[1,*], Attila Ábrahám[2], László Szabó[3], Ervin Gy. Szabó[3], Sándor Stichleutner[1], Ernő Kuzmann[4], Zoltán Homonnay[4], Gyula Tolnai[5]

[1] *Centre for Energy Research, Hungarian Academy of Sciences, Konkoly Thege Miklós út 29-33, 1121 Budapest, Hungary*

[2] *Centre for Colloid Chemistry, Budapest University of Technology and Economics, 1111 Budapest, Budafoki út 6-8, Hungary*

[3] *Research Centre for Natural Sciences, Hungarian Academy of Sciences, Magyar tudósok körútja 2, 1117 Budapest, Hungary*

[4] *Institute of Chemistry, Eötvös Loránd University, Pázmány P. s. 1/A, 1117 Budapest, Hungary*

[5] *Kondorosi út 8/A., 1116 Budapest, Hungary*

Abstract. Chemical stability and good biocompatibility under physiological conditions render nanoparticles made of the spinel oxide magnetite a favorable choice in biomedical diagnostic and therapeutic applications that benefit from high levels of magnetization and superparamagnetism. Under ambient atmosphere, however, magnetite nanoparticles are prone to undesired oxidation leading to an at least partially oxidized form of magnetite. In the present work $Fe_{3-x}O_4$ nanopowders (with a particle size of 10-50 nm) were prepared under different conditions via chemical co-precipitation method, resulting in samples with different oxidation levels. The effect of oxidation of the prepared samples on their morphological, structural, electronic and magnetic properties is followed, respectively, by the means of transmission electron microscopy (TEM), powder X-ray diffractometry (PXRD), ^{57}Fe Mössbauer spectroscopy (MS) and electron magnetic resonance (EMR) spectroscopy measurements. A novel method is applied to decompose the heavily broadened room-temperature ^{57}Fe Mössbauer spectra of the nanoparticles into signals of intermediate valence $Fe^{2.5+}$ and that of Fe^{3+} iron species. The results indicate that the cubic lattice parameter of non-stoichiometric magnetite nanoparticles depends on the concentration as well as on the mean oxidation level of the intermediate valence iron species. At the same time, EMR spectra of the samples indicate that oxidation influences the magnetic anisotropy of the nanoparticles, with the magnitude of the nanoparticles' magnetic anisotropy field being correlated with the concentration of the intermediate valence iron species. Malic acid, used as coating agent for several of the samples, is shown to hinder the oxidation of magnetite nanoparticles.

Keywords: nanoparticles; magnetite; hyperfine interactions; Mössbauer spectroscopy; electron magnetic resonance

*Corresponding author, e-mail: klencsar.zoltan@energia.mta.hu

1. INTRODUCTION

Their small size, high surface area fraction and unique electronic and magnetic properties can render magnetic nanoparticles useful for various application purposes [1,2]. Among them, magnetite nanoparticles are found to be exceedingly useful in application fields such as catalysis [3], environmental remediation [4], biomedical diagnostic and therapeutic applications [5] as well as biological tissue engineering [6]. Magnetite nanoparticles are a favorable choice in these applications on account of their advantageous material properties, such as high Curie-temperature, high levels of magnetization, superparamagnetism along with chemical stability, low toxicity and good biocompatibility under physiological conditions, among others [1,5]. However, magnetite has long been known to be prone to oxidation under ambient atmosphere [7,8,9], leading to partially oxidized, non-stoichiometric magnetite, to maghemite, or to a mixture of the two as intermediate product [8]. The effect of oxidation can be especially pronounced in the case of nanoparticles that display an enhanced surface to volume ratio with respect to larger-size particles [8,9]. Though maghemite and non-stoichiometric magnetite do share some of the advantageous properties of magnetite [10], there are also key differences [11] that make unambiguous characterization of corresponding particles desirable from the applications point of view: while the saturation mass magnetization of magnetite (92-100 Am^2/kg) exceeds that of maghemite (60-80 Am^2/kg) by a considerable margin [2,9,12], the magnitude of first order magnetic anisotropy is also known to decrease with decreasing Fe^{2+} concentration in non-stoichiometric magnetite [13]. These physical properties are especially important in the field of biomedical applications [5]. At the same time, the reducing ability of magnetite, considered in the reduction of aqueous contaminants, has also been shown to decrease with increasing levels of cation non-stoichiometry [14]. In order to determine the suitability of magnetite nanoparticles and the corresponding preparation and handling procedures for a particular application area, it is therefore desirable that they are reliably characterized regarding their oxidation state and associated properties.

To assess material properties related to the oxidation state of iron oxide particles, one may turn to several different spectroscopic methods, such as, e.g., ^{57}Fe Mössbauer spectroscopy [7,8,9,11], Raman spectroscopy [15], X-ray photoelectron spectroscopy [16] and X-ray

absorption spectroscopies [17]. Concerning the composition of iron oxides with respect to iron ions in different valence states, ^{57}Fe Mössbauer spectroscopy may be considered as one of the most commonly used techniques to gain relevant information about iron oxide samples [11], and it is frequently the method of choice in investigations regarding nanomaterials [9]. However, while bulk maghemite and magnetite can be indeed well distinguished on the basis of their room-temperature ^{57}Fe Mössbauer spectra [8,18], when prepared in the nanoparticle form, various levels of oxidation combined with relaxation effects, such as collective magnetic excitation, complicates the room-temperature ^{57}Fe Mössbauer spectrum of (nominally) magnetite nanoparticles in a way that makes it questionable whether and to what extent the studied sample can be regarded as magnetite, non-stoichiometric magnetite, maghemite or a mixture of these phases. Furthermore, overlapping of Fe^{3+} Mössbauer spectral components associated with maghemite and magnetite can make the results of corresponding quantitative analysis of mixture and solid solution samples inconclusive [8].

Similarly, X-ray diffractograms of magnetite nanoparticle powders are usually characterized by broad reflection peaks on account of the small crystallite size, and reflections that could serve as the basis of distinction between magnetite and maghemite (due to vacancy ordering in the latter [11]) can be small and broadened enough to be lost in the statistical noise of the measurement [8]. Additional broadening due to a strain in the lattice parameter reflecting a distribution in the oxidation level and iron concentration attributes of the nanoparticles can stand in the way of an unambiguous X-ray diffractometry based phase analysis, too.

While lowering the sample temperature will in general reduce thermally agitated relaxation effects and associated broadening in the Mössbauer spectra [11], application of an external magnetic field may have a similar effect [19] beside promoting the separation of subcomponents associated with iron ions having opposite spin directions [20]. However, lowering the temperature of magnetite will induce a structural (cubic to orthorhombic [21]) and electronic (metal to insulator [22]) transition at ~ 120 K (Verwey transition), which is accompanied by associated changes in the magnetic properties [23] and leads to further complications of the Mössbauer spectral pattern [11]. In this respect an additional source of uncertainty arises due to the Verwey transition temperature being reduced in correlation with decreasing particle size [24] as well as with increasing non-stoichiometry [25] of magnetite.

In addition, measuring spectra at the temperature of the boiling point of liquid nitrogen (~ 77 K) may also turn out to be impractical on account of an unsuitability of low-temperature spectra for providing conclusive proofs concerning the concentration of magnetite along with its partly or fully oxidized counterparts in the sample [8]. Measuring below room temperature in order to reduce relaxation effects, but at the same time above the Verwey transition temperature in order to avoid associated complications of the spectral shape may help spectrum decomposition by reducing line broadening [11]. At the same time, lowering the temperature is also expected to result in an additional broadening of absorption peaks associated with intermediate valence iron ions subject to electron hopping at octahedral sites in magnetite [26].

Placing the sample in external magnetic field, while it may improve separation of ^{57}Fe Mössbauer spectral components associated with iron ions situated at octahedral and tetrahedral sites, does not necessarily cancel apparent broadening effects [19] related to magnetic relaxation, particle size distribution, non-stoichiometric compositions and magnetite-maghemite phase mixtures. At the same time, it can introduce an additional source of ambiguity related to the degree of magnetic polarization of iron ions situated in the multitude of different microenvironments, and in powders it may also contribute to line broadening due to the random orientation of the crystallites with respect to that of the applied magnetic field.

In general, due to the complexity of corresponding ^{57}Fe Mössbauer spectra, for non-stoichiometric magnetite/maghemite nanoparticle systems the application of an external magnetic field and/or the measurement at low temperatures while able to provide additional information about the studied sample, do not necessarily ensure achievement of an unambiguous result concerning the sample composition [20]. Improvement of reliability of corresponding results derived on the basis of more readily accessible room-temperature ^{57}Fe Mössbauer spectra would therefore be desirable. One should also consider that especially in the case of biomedical applications, the room-temperature material properties can be seen as being more relevant from the applications' point of view than those characterizing the nanoparticles at lower temperatures.

In the present work we contribute to this field by investigating the effect of preparation conditions on structural, morphological and magnetic properties of $Fe_{3-x}O_4$ nanoparticles, and

by presenting a quasi model-independent method of analysis for the decomposition of room-temperature ^{57}Fe Mössbauer spectra that display considerable broadening and overlapping of absorption peaks. Through a consistent analysis of experimental results observed by the methods of transmission electron microscopy (TEM), powder X-ray diffractometry (PXRD), electron magnetic resonance (EMR) spectroscopy and ^{57}Fe Mössbauer spectroscopy (MS), we demonstrate that by using the proposed model, one can achieve reasonable decomposition and analysis of room-temperature ^{57}Fe Mössbauer spectra of $Fe_{3-x}O_4$ nanoparticle systems even in the presence of excessive absorption line broadening caused by collective magnetic excitation and partial oxidation of magnetite nanoparticles.

2. EXPERIMENTAL

2.1. Synthesis

Fe_3O_4 nanopowders were prepared via chemical co-precipitation method starting from mixed solution of Fe^{2+} and Fe^{3+} salts in strongly alkaline aqueous medium. $FeSO_4 \cdot 7\ H_2O$ and $FeCl_3 \cdot 6\ H_2O$ were used as reagent grade metal precursors and NaOH for pH adjustment in starting solutions. In a typical synthetic procedure, 17.15 g $FeSO_4 \cdot 7\ H_2O$ and 35.5 ml $FeCl_3$ solution (3.50 M) were dissolved in 500 ml distilled water. 53.0 mg of malic acid dissolved in 200 ml distilled water was then added as coating agent in case of the samples M3a, M3b and M4, while for the rest of the samples a corresponding amount of distilled water was added without the acid. The pH was then adjusted using NaOH solution prepared by dissolving 20.7 g NaOH in 200 ml distilled water. After the alkaline solution was added, the color of the solution changed from orange to black rapidly. In the next step the reaction mixture was homogenized via vigorous stirring for 15 minutes at room temperature either under air (samples M2, M4) or under nitrogen atmosphere (samples M1a, M1b, M3a, M3b). The solution was heated to reflux at 100°C for 2 hours. After the reaction was completed, the obtained particles were filtered and purified by washing several times with distilled water, and then dried either at room temperature (samples M1a, M3a) or at 80°C (samples M1b, M2, M3b, M4).

The samples for ^{57}Fe Mössbauer spectroscopy were prepared by evenly distributing 10 mg of the prepared powders over a collimated area of 0.5 cm^2, and then fixing the sample

geometry thus achieved by pouring melt paraffin wax over the area in question. The resulting samples had approximately 14.4 mg/cm^2 surface density of natural iron.

Electron magnetic resonance (EMR) spectroscopy measurements were carried out at room temperature on 0.1 mg nanoparticle powder evenly mixed with 19.9 mg KBr in order to realize a steady random powder geometry.

2.2. Characterization

Powder X-ray diffraction patterns of the powders were obtained at room temperature either with a Philips X'Pert diffractometer (sample M1b) or with a Philips PW3710 based PW1050 Bragg-Brentano parafocusing goniometer (all other samples), by using Cu K_α radiation, graphite monochromator and proportional counter. The scattering angle 2θ was adjusted in the range of 20…85 deg in step scan mode with a step size of 0.04 deg and a counting time of 1 s per step. The lattice parameters and the characteristic crystallite size of the nanoparticles were determined by fitting the diffraction peaks to Lorentzian functions with position and full width at half maximum (FWHM) parameters determined on the basis of Bragg's law and Scherrer's equation [27], respectively, the latter being used in the form of

$$\Gamma_+(2\theta)/\mathrm{deg} = \frac{180}{\pi}\frac{0.9\lambda}{d\cos\theta}\ ,\quad \Gamma(2\theta) = \Gamma_0 + \Gamma_+(2\theta) \tag{1}$$

where d is the characteristic size (diameter) of the crystallites, $\lambda \approx 0.154186$ nm is the wave length of the applied Cu K_α radiation, $\Gamma(2\theta)$ denotes the full width (FWHM) of the diffraction peak associated with the scattering angle 2θ, and $\Gamma_0 = 0.11$ deg accounts for instrumental broadening.

Electron magnetic resonance (EMR) measurements were carried out on a Bruker ElexSys E500 X-band spectrometer. Unless otherwise noted, the conditions of EPR measurements involved a modulation frequency of 100 kHz, modulation amplitude of 1 G, microwave power of 0.02 mW and microwave frequencies of $f \approx 9.85$-9.86 GHz. The spectra were scanned twice in the magnetic field range of 100...10900 G with sweep time of ~ 84 s. The magnetic field axis of the spectra obtained was rescaled to $f_0 \approx 9.85$ GHz (i.e. abscissa values were multiplied by f_0/f) for analysis and further processing.

Transmission electron microscopy (TEM) measurements were carried out on the powdered samples by a Morgagni 268D instrument operating at 100 kV.

^{57}Fe Mössbauer spectra of powdered samples were recorded in transmission geometry by using conventional spectrometers (Wissel) operated in constant acceleration mode along with a ^{57}Co(Rh) radioactive source providing the γ-rays with ca. 20 mCi activity. ^{57}Fe isomer shift values are given relative to that of α-iron at room temperature. The spectra were analyzed by assuming the nuclear gyromagnetic factors of $g_e = -0.103267$ and $g_g = +0.18088$ for the excited ($I_e = 3/2$) and ground ($I_g = 1/2$) state of the ^{57}Fe nucleus.

^{57}Fe Mössbauer spectra and X-ray diffractograms were analyzed by using version 4.0 of the MossWinn program [28,29] that was complemented with auxiliary libraries providing the fitting functions for the PXRD measurements.

3. RESULTS AND DISCUSSION

On the basis of their TEM images (Figure 1) the prepared powder samples are composed of nanoparticles with a typical particle size range of 10-20 nm, with the exception of sample M1b in which case particles with a size of ~ 50 nm can be observed. Magnetic interactions among the particles are visualized in the tendency of the individual particles to form larger agglomerates with a characteristic diameter of 200-500 nm. The causes for the larger particle size of sample M1b in comparison with that of M1a and M3b may involve the drying at higher temperature and the preparation without coating agent. As for the samples prepared with coating agent applied (M3a, M3b, M4), the coating agent malic acid becomes adsorbed onto the surface of magnetite nanoparticles during synthesis, with their carboxyl groups being deprotonated due to the strongly alkaline aqueous medium, which can prevent the formation of larger particles by hindering aggregation of the particles via electrostatic repulsion.

Powder X-ray diffractograms of the samples (Figure 2) confirm the formation of the cubic spinel phase in each case. The values of the lattice parameter and the average crystallite size, as obtained from the fit of the diffractograms according to Bragg's law and Scherrer's equation, are depicted in Figure 3. With the exception of sample M1b, the average crystallite size of the nanoparticles corresponds well to the characteristic particle size, suggesting that the corresponding powders are composed mainly of single crystallites. In contrast, the larger particles of sample M1b are polycrystals that have formed from crystallites of the same size as that found in the rest of the powders. Concerning the average crystallite size, there is a clear distinction between samples that were prepared with a coating agent (M3a, M3b, M4) and

those that were prepared without it (M1a, M1b, M2): the application of malic acid as coating agent apparently leads to the formation of larger crystallites (Figure 3). The cubic lattice parameter is significantly lower than that of bulk magnetite ($a \approx 0.8396$ nm) for all of the samples, and the lattice parameter of sample M1b is actually only marginally larger than that of bulk maghemite ($a \approx 0.834$ nm) [11].

The X-band electron magnetic resonance spectra (Figure 4) display broad ferromagnetic resonance (FMR) signals for each of the samples. The spectra are asymmetric (they are more shallow around their minimum than around their maximum) as expected for magnetic crystals displaying (negative) cubic magnetocrystalline anisotropy such as magnetite (at room temperature). There are also subtle differences among the magnetic field values at which the maximum level of absorption (where the measured derivative curves cross zero around $B \approx 3000$ G) can be observed for the different samples. Following [30], main features of such spectra may be described with their asymmetry ratio A and effective spectroscopic splitting factor g_{eff}. Definitions of these parameters in terms of the ferromagnetic resonance signal are given in Figure 5.

The asymmetry ratio values obtained (on the basis of the spectra displayed in Figure 4) for the different samples are depicted as a function of the respective g_{eff} values in Figure 6. On the one hand, all the samples display an asymmetry ratio that is higher than 1.0, which is the expected behavior for crystallites with negative first order cubic magnetocrystalline anisotropy. On the other, A displays a near linear dependence on the value of g_{eff}, which suggests that both quantities depend on a single underlying physical parameter. Indeed, spectra associated with powders of magnetic crystals characterized by different negative first order cubic magnetic anisotropy fields (B_{a}) [31,32] (assuming other attributes of the crystals remain the same) can lead to such correlated differences in the values of A and g_{eff}: an increase in $|B_{\mathrm{a}}|$ will lead to the simultaneous increase of A and g_{eff}. It follows that from the point of view of the profile of the X-band electron magnetic resonance spectra, the main difference among the prepared samples lies in the different values of the cubic magnetic anisotropy fields associated with the corresponding crystallites. According to Figure 6, the largest absolute magnetocrystalline anisotropy field is observed for sample M3a, and the lowest for sample M2.

Magnetocrystalline anisotropy can be expected to depend on the structure and composition of the crystallites. Via moderate spin-orbit coupling, high-spin Fe^{2+} ions can contribute to magnetocrystalline anisotropy in magnetite [33], which explains why decreasing Fe^{2+} concentration leads to a decreasing magnitude of the first-order magnetocrystalline anisotropy in non-stoichiometric magnetite [13]. Thus, if our samples would differ exclusively in their Fe^{2+} concentration, one could expect samples with higher A and g_{eff} values to be closer in composition to magnetite. On the basis of Figure 6, this would then reveal sample M3a as the most magnetite-like and sample M2 as the most maghemite-like (most oxidized) nanoparticle powder among those investigated. In relation to these two particular samples, the comparison of corresponding cubic lattice parameters indeed appears to support this conclusion. This is not the case, however, for all of the possible sample pairs. For example, sample M1b is characterized by a smaller lattice parameter, but at the same time by larger A and g_{eff} values than M1a.

A possible reason for this could be the difference in the characteristic particle size of the two samples. Namely, for nanoparticles which are small enough to have their magnetic moment being subject to thermally induced relaxation, the apparent volumetric magnetic anisotropy will decrease with increasing rate of the relaxation, reaching zero in the superparamagnetic state [32]. Given that magnetic relaxation phenomena are expected to take place in our samples at room temperature, the apparent cubic magnetocrystalline anisotropy field reflected by the A and g_{eff} values obtained (Figure 6) could depend on the particle size as well. Among particles with identical composition, magnetic relaxation will be more suppressed for larger particles that may therefore display a higher apparent cubic magnetocrystalline anisotropy field, with correspondingly higher A and g_{eff} values. This could explain why sample M1b with the largest particle size displays higher A and g_{eff} values than M2, M1a and M4 (Figure 6), despite having a composition closest to maghemite among these samples on the basis of its cubic lattice parameter (Figure 3). In addition, a similar effect can also be observed in the case of samples M4, M3b and M3a, for which the increasing crystallite size (in the given order) is accompanied by increasing A and g_{eff} values, even though the respective cubic lattice parameters do not follow a similarly consistent tendency.

Though the above observations appear to point to the importance of a size-related magnetic relaxation effect in determining the values of A and g_{eff}, in the present case we do not expect

magnetic relaxation effects to have an appreciable influence on the measured EMR spectra (and the associated parameters) on account of the roughly 2 orders of magnitude shorter time scale (with respect to that of ^{57}Fe Mössbauer spectroscopy) at which EMR spectroscopy in the X-band (in the 9-10 GHz microwave frequency range) samples the magnetic state of the nanoparticles. Namely, due to this shorter time scale, at a given relaxation frequency magnetic relaxation effects are expected to have milder influence on the EMR spectra than they do on ^{57}Fe Mössbauer spectra, and even in the case of the latter (Figure 7) we observe only the effects of collective magnetic excitations (as opposed to superparamagnetism). As an example, we note that even when ^{57}Fe Mössbauer spectra display superparamagnetic behavior of nanoparticles, X-band EMR spectra may still show clear signs of the particles' magnetic anisotropy (compare, e.g., Figures 4 and S6 in [36]). Therefore, for the present samples we do not expect differences in the particle size to have notable influence on the trend reflected by the A asymmetry ratio (Figure 6), but further on we rather put forward another possible explanation for the discrepancies observed between the tendencies reflected by the cubic lattice parameter and the EMR parameter values.

Concerning the EMR measurements, it is also worth to note that on the basis of the (A,g_{eff}) value pairs obtained (Figure 6) the present samples correspond to the same region as that typically spanned by synthetic magnetites and maghemites along with biologically induced magnetites according to [30].

Room-temperature ^{57}Fe Mössbauer spectra of the samples are displayed in Figure 7. Neither of the spectra reveals well separated sextet components that could be identified as originating from iron at tetrahedral or octahedral sites in magnetite. The broadening that causes the heavy overlap of the absorption peaks may in part be attributed to the non-stoichiometry of magnetite. Namely, the latter can result in a strain in the electronic state (and thus in a distribution in the corresponding values of the hyperfine magnetic field and/or the ^{57}Fe isomer shift) of iron ions mainly at the octahedral site of the spinel, transforming some of the octahedral $Fe^{2.5+}$ iron species of ideal magnetite, e.g., to octahedral Fe^{3+}. At the same time, the broadened peaks of the sextet features display inward shoulders that are typical for the relaxation phenomenon of collective magnetic excitations in the presence of a strain in the magnetic anisotropy energy barrier of the individual nanoparticles, which latter may be caused by a moderate distribution in the particle size, for example. Such type of relaxation

causes a distribution in the hyperfine magnetic fields (HMF), extending from a maximum value—characteristic to the largest particles—towards lower values associated with smaller particle sizes. Due to this HMF distribution the subcomponents associated with octahedral and tetrahedral iron ions are both broadened considerably. Such spectra can be decomposed into individual subcomponents in many different ways depending on the presumptions made about the sample and realized in the form of the selected fit model. Among others, the spectrum of samples M2 and M4 can be decomposed with high accuracy for example into four broadened sextet components as we have shown previously [34]. While most such decompositions will reflect some part of the true nature of the corresponding samples (such as M4 being closer to the state of magnetite than M2 [34]), in the case of spectra displaying as heavy overlaps of the absorption peaks as displayed in Figure 7, any of such decompositions will raise the question as to what extent were the final results obtained solely due to the particularities of the fit model applied. This can prevent the unambiguous detailed decomposition of the spectra into separate components associated with Fe^{3+} and $Fe^{2.5+}$. (We use the notation '$Fe^{2.5+}$' to refer to all possible iron species subject to fast electron hopping and characterized consequently by a valence state intermediate between Fe^{3+} and Fe^{2+}, irrespective of whether their intermediate valence is exactly 2.5+ or not.) A possible way to alleviate the mentioned ambiguity is to turn to so called 'model independent' methods [35] that can be used even without advance knowledge concerning the number of distinct components that contribute to the measured spectrum. This typically enables one to reduce the number and simplify the nature of assumptions incorporated into the fit model, which can lead (provided that the simplified assumptions are essentially correct) to results that are more definite than those achieved on the basis of a presumed number of discrete subcomponents. In the present case a multitude of magnetic sextet components may be expected to contribute to the measured spectra (Figure 7) due to distributions mainly in the ^{57}Fe hyperfine magnetic field and ^{57}Fe isomer shift (IS) Mössbauer parameters that are sensitive messengers of the relaxation state (here mainly the HMF) and the oxidation state (both IS and HMF) of iron ions. One can expect the highest variability in the HMF parameter, and consequently one may consider to describe the spectra by assuming a powder sample with a distribution in the hyperfine magnetic field, along with a single ^{57}Fe isomer shift parameter common to all the fitted sextet components. One can readily apply such a fit model to the present spectra, which leads to a fair fit with a common

isomer shift value of around ~ 0.34 mm/s, reflecting the presence of Fe^{3+} only, and characterizing all the samples essentially as being composed of fully oxidized magnetite / maghemite nanoparticles subject to collective magnetic excitations.

The differences we detected among the samples concerning the cubic lattice parameter (Figure 3) and the magnetic anisotropy related EMR spectrum parameters (Figure 6), however, indicate that there must be larger differences among the spectra regarding their level of oxidation, and the presence of $Fe^{2.5+}$ must therefore be assumed in the corresponding ^{57}Fe Mössbauer spectra, meaning that the assumption of a single ^{57}Fe isomer shift value for all the spectral components is not a reasonable one. This consideration calls for a fit model that includes at least two overlapping magnetic subcomponents with possibly different isomer shift values, each displaying a hyperfine magnetic field distribution. For the present case, we set up a corresponding fit model as follows.

Decomposition of the Mössbauer spectra into overlapping components is in general prone to correlations among the amplitudes associated with the individual components. A possible way to reduce the uncertainty caused by such correlations is to apply—physically reasonable—constraints to the fit model. A commonly applied and acceptable such constraint is to assume line widths of all Lorentzians the model is composed from to be the same. Any differences in line broadening may then be covered (formally) by the HMF distributions themselves. Another constraint that we have applied is defined by the assumption that any differences between the isomer shifts of different Fe^{3+} and those between different $Fe^{2.5+}$ species can be neglected in comparison to the differences between the isomer shift values of Fe^{3+} and $Fe^{2.5+}$ species. This means that for each spectrum a single Fe^{3+} isomer shift value and a single $Fe^{2.5+}$ isomer shift value can be assumed, and any spread in the isomer shift values associated with Fe^{3+} and $Fe^{2.5+}$ species must be (formally and approximately) accounted for by corresponding broadening in the respective HMF distributions. In addition, we have assumed that the oxidation level of the samples influence mainly the isomer shift and the relative area fraction of the $Fe^{2.5+}$ components, without having appreciable effect on the isomer shift of the Fe^{3+} species. Accordingly, in our model we have constrained the isomer shift of Fe^{3+} components to have the same (fitted) value for all the six spectra (Figure 7).

Applying the above constraints essentially means that we make an attempt to explain differences between the measured spectra in terms of differences between the isomer shifts of

intermediate valence iron species and the corresponding spectral area fractions, as well as in terms of differences between the Fe^{3+} and $Fe^{2.5+}$ HMF distribution profiles.

The fit parameters resulted from such a constrained fit are listed in Table 1, and the corresponding fit envelopes are displayed in Figure 7. The hyperfine magnetic field distributions derived for the Fe^{3+} and $Fe^{2.5+}$ components are displayed in Figure 8. Figure 9 displays the $Fe^{2.5+}$ component isomer shift as a function of the spectral area fraction of the same component for the different samples.

The latter figure indicates that our approach of fitting successfully captured the essence of the differences between the samples and the associated spectra. Namely, on the one hand, the largest isomer shift values are obtained for the samples (M3a, M3b, M4) that were prepared with coating agent and—among the present samples—they are closest to realize the state of magnetite on the basis of their cubic lattice parameter (Figure 3). The $Fe^{2.5+}$ isomer shift obtained for sample M4 is ~ 0.66 mm/s, a value that is typical for magnetite [18], though in the context of the present samples this value appears to be an outlying one. The relative area fraction of the $Fe^{2.5+}$ component is also largest in the case of these samples. Apart from M4, it appears that on oxidation of the samples both the isomer shift and the relative area fraction of the $Fe^{2.5+}$ component is reduced. A possible explanation for the outlying nature of sample M4 is that this particular sample may be a mixture of (perfect) magnetite and maghemite, as opposed to being a non-stoichiometric magnetite, which latter state is probably better realized by the rest of the samples. This view concerning sample M4 is also corroborated by the changes caused by aging in the corresponding ^{57}Fe Mössbauer spectrum (Figures S1-S3). Overall, the results clearly reflect that malic acid applied as coating agent hinders oxidation of the nanoparticles.

The applied decomposition of the Mössbauer spectra is further confirmed by the correlation between the relative area fraction of the $Fe^{2.5+}$ component and the cubic lattice parameter (Figure 10) of the samples. One can also detect similarities between the dependence of the lattice parameter (Figure 10) and that of the ^{57}Fe isomer shift (Figure 9) on the $Fe^{2.5+}$ component relative area fraction, suggesting that the lattice parameter is also correlated with the isomer shift of the intermediate valence iron ions, which is indeed confirmed as shown in Figure 11. A lower isomer shift value and a lower area fraction of the $Fe^{2.5+}$ component can both refer to a reduced Fe^{2+}/Fe^{3+} ratio, and thus to an enhanced level of

oxidation in the samples. Assuming, as in [11], that the $x_{MS} = Fe^{2+}/Fe^{3+}$ ratio can be estimated as

$$x_{MS} = \frac{½\,Fe^{2.5+}}{Fe^{3+} + ½Fe^{2.5+}} \tag{2}$$

where the ion symbols stand for the corresponding area fractions in the measured Mössbauer spectra (i.e. $Fe^{3+} + Fe^{2.5+} = 1$), we find a correlation between x_{MS} and the cubic lattice parameter as shown in Figure 12(a), where a similar axis range is used as in Figure 7 of reference [11] (displaying a correlation of similar nature for numerous non-stoichiometric magnetite samples) in order to facilitate comparison. Apart from sample M1b, the correlation found for our samples shows fair agreement with the one depicted in the latter figure [11], corroborating that our chosen fit method provided reasonable values for the relative area fraction of the $Fe^{2.5+}$ component in the different samples. However, the outlying nature of M1b suggests that it may also be necessary to take the isomer shift of the latter component into account when calculating the Fe^{2+}/Fe^{3+} ratio for a given sample. Namely, with respect to Eq. (2) it would be justifiable to attribute lower Fe^{2+} concentration to those samples that show an $Fe^{2.5+}$ isomer shift below that (0.66 mm/s [18]) characteristic to perfect magnetite. As a first approximation, the equivalent Fe^{2+} concentration may be assumed to depend linearly on the $Fe^{2.5+}$ isomer shift, leading to a corresponding modified expression of

$$x_{MS,\delta} = \frac{½\,q(\delta)Fe^{2.5+}}{Fe^{3+} + (1-½\,q(\delta))Fe^{2.5+}} = \frac{q(\delta)Fe^{2.5+}}{2-q(\delta)Fe^{2.5+}} \tag{3}$$

with

$$q(\delta) = \frac{\delta - \delta_{min}}{\delta_{max} - \delta_{min}}\,, \tag{4}$$

where the index δ was introduced in $x_{MS,\delta}$ in order to distinguish the corresponding values from x_{MS} of Eq. (2). Assuming $\delta_{max} = 0.66$ mm/s (see above, [18]), and the cubic lattice parameters of $a = 0.8339$ nm and $a = 0.8394$ nm [11] for maghemite ($x_{MS,\delta} = 0.0$) and magnetite ($x_{MS,\delta} = 0.5$), respectively, along with a hypothetical strictly linear dependence of a on $x_{MS,\delta}$, by considering the cubic lattice parameter and $Fe^{2.5+}$ isomer shift values obtained for the present samples we aimed at finding δ_{min} such that the corresponding $x_{MS,\delta}$ values provide

the lowest squared deviation from the hypothesized linear dependence. The corresponding calculations led to $\delta_{\min} \approx 0.372$ mm/s, which is a reasonable value given that it lies between the room-temperature isomer shift values associated with Fe^{3+} situated at the octahedral site in maghemite (0.36 mm/s) and in non-stoichiometric magnetite (0.39 mm/s) [18]. The $x_{MS,\delta}$ approximation of the samples' Fe^{2+}/Fe^{3+} ratio based on this $\delta_{\min}$ value can be calculated according to Eqs. (3) and (4), by using the obtained $Fe^{2.5+}$ isomer shift values as given in Table 1. The dependence of the cubic lattice parameter on the calculated $x_{MS,\delta}$ values is shown in Figure 12(b). As expected on the basis of its relatively low isomer shift value (Figure 9), in this case sample M1b fits better in the overall trend set by the rest of the samples. Furthermore, the correlation between the cubic lattice parameter and $x_{MS,\delta}$ is closer to the expected behavior (as reflected by Figure 7 of reference [11]) than the one displayed in Figure 12(a), which finding corroborates our approach concerning the role of the isomer shift of the $Fe^{2.5+}$ component in determining the formal Fe^{2+}/Fe^{3+} ratio in these samples.

Figure 13 displays the *A* asymmetry ratio EMR parameter as a function of the $Fe^{2.5+}$ component's relative spectral area. Apart from sample M4 that counts here again as an outlying case, the asymmetry ratio, and thus the magnitude of the magnetic anisotropy field shows a positive, near linear correlation with the Mössbauer spectrum area fraction of the $Fe^{2.5+}$ component. On the basis that decreasing Fe^{2+} concentration should lead to a decreased magnetocrystalline anisotropy magnitude in non-stoichiometric magnetite [13], this is indeed the expected nature of interdependence between these quantities. Apparently, with the exception of sample M4, differences in the relative area fraction of the $Fe^{2.5+}$ component can explain the differences found in the *A* asymmetry ratio (Figure 6), which suggests that the isomer shift of the $Fe^{2.5+}$ component does not have a strong influence on *A*. In contrast, the cubic lattice parameter was found to correlate with the mean isomer shift of the $Fe^{2.5+}$ component (Figure 11), which correlation may then be at the root of the formerly mentioned discrepancy found between the trends reflected by the *A* asymmetry ratio (Figure 6) and the cubic lattice parameter values (Figure 3). Namely, provided that a higher concentration of intermediate valence $Fe^{2.5+}$ is accompanied by a reduced isomer shift value of the same iron species (and thus by a mean oxidation state closer to that of Fe^{3+}), a change in the *A* asymmetry ratio is not necessarily accompanied by a corresponding change in the cubic lattice parameter. Among the present samples, M1b represents an example for such a behavior, as

reflected by its outlying nature on Figure 9. This may be connected to the larger size of its particles that display a reduced specific surface area in comparison with the remaining samples. Namely, in its case a larger concentration of iron ions resides in the interior volume of the particles, than in the case of the rest of the samples, which should tend to promote preservation of a higher fraction of iron ions in an intermediate valence state.

The effect of drying the powders at higher (80°C) temperature can be elucidated by comparing attributes of samples M1a and M1b (both prepared without coating agent) as well as those of M3a and M3b (both prepared with coating agent). On the basis of Figure 11 it is clear that drying at 80°C (M1b and M3b) leads to a lower $Fe^{2.5+}$ isomer shift value along with a lower cubic lattice parameter than drying at room temperature (M1a and M3a), i.e. it promotes oxidation of the samples. While the sample pair prepared with coating agent (M3a, M3b) is closer to the state of being magnetite than the pair prepared without it (M1a, M1b), the presence of coating agent does not seem to alleviate the enhancement of oxidation caused by drying at higher temperature. As for the case of the sample pair (M3a, M3b), the corresponding magnetic anisotropy fields reflected by the FMR data depicted in Figure 6 corroborate that the state of M3a is closer to magnetite than that of M3b. On account of the lower $Fe^{2.5+}$ isomer shift being accompanied by a larger $Fe^{2.5+}$ concentration in sample M1b (Figure 9), the same kind of comparison remains inconclusive concerning the pair (M1a, M1b).

4. CONCLUSIONS

Magnetite nanoparticles, having a crystallite size in the order of 10-20 nm and being subject to different levels of oxidation, are characterized by room-temperature ^{57}Fe Mössbauer spectra displaying spectral broadening caused by the simultaneous presence of non-stoichiometry and thermally activated collective magnetic excitations. On the basis of their ^{57}Fe Mössbauer spectra the different oxidation levels of the nanoparticle samples can be followed mainly in terms of differences between the mean isomer shifts of intermediate valence iron species and the corresponding spectral area fractions. The sum of two spectrum components displaying hyperfine magnetic field distributions with different characteristic isomer shifts appears to be a suitable model for the extraction of these differences from the ^{57}Fe Mössbauer spectra, provided that the latter are evaluated simultaneously by applying

physically reasonable constraints that are able to alleviate uncertainties related to parameter correlations arising from the overlap of the fitted components. Our results consistently reveal that application of the coating agent malic acid during preparation hinders oxidation of magnetite nanoparticles and leads to larger crystallites than the same preparation route without the coating agent applied. Compared to particles dried at room temperature, drying the as prepared nanoparticles at higher (80°C) temperature leads to their more pronounced oxidation, which effect takes place regardless of the application of the coating agent. Correlations among Mössbauer-, PXRD and EMR parameters suggest that oxidation of magnetite nanoparticles may result in an increase of the mean oxidation level of the intermediate-valence iron ions as well as in a decrease of their concentration, with the relative magnitude of the two effects possibly being influenced by the particle size. While the cubic lattice parameter appears to correlate with the concentration as well as with the mean oxidation level of the intermediate valence iron species in non-stoichiometric magnetite, the nanoparticles' magnetic anisotropy field, as reflected by EMR spectroscopy measurements, is mainly influenced by the concentration of the iron species in question.

The present results also underline the ability of EMR spectroscopy to reflect oxidation-born deviations from the ideal magnetite stoichiometry in nanoparticle samples of non-stoichiometric magnetite, and to distinguish in this respect corresponding samples with different oxidation levels.

Acknowledgements

This work was supported by the Hungarian National Research, Development and Innovation Office – NKFIH (K115784 and K115913). Technical help of Mrs. Lászlóné Millián is gratefully acknowledged. Z.K. expresses thanks to Prof. Ferenc Simon (Institute of Physics, Budapest University of Technology and Economics, Budapest, Hungary) for making available the applied spectrometer for recording the EMR spectra.

References

[1] L. Mohammed, H.G. Gomaa, D. Ragab, J. Zhu: *Particuology* **30** (2017) 1-14.

[2] D. Ramimoghadam, S. Bagheri, S. Bee, A. Hamid: *Colloids and Surfaces B: Biointerfaces* **133** (2015) 388-411.

[3] A.C.C. Arantes, C.G. Almeida, L.C.L. Dauzacker, M.L. Bianchi, D.F. Wood, T.G. Williams, W.J. Orts, G.H.D. Tonoli: *Carbohydrate Polymers* **163** (2017) 101-107.

[4] S. Bagheri, N.M. Julkapli: *Reviews in Inorganic Chemistry* **36** (2016) 135-150.

[5] A. Figuerola, R. Di Corato, L. Manna, T. Pellegrino: *Pharmacol. Res.* **62** (2010) 126-143.

[6] K. Shimizu, A. Ito, M. Arinobe, Y. Murase, Y. Iwata, Y. Narita, H. Kagami, M. Ueda, H. Honda: *Journal of Bioscience and Bioengineering* **103** (2007) 472-478.

[7] A. Gedikoqlu: *Scripta Metallurgica* **17** (1983) 45-48.

[8] G.M. da Costa, C. Blanco-Andujar, E. De Grave, Q.A. Pankhurst: *J. Phys. Chem. B* **118** (2014) 11738-11746.

[9] C. Rümenapp, F.E. Wagner, B. Gleich: *J. Magn. Mag. Mater.* **380** (2015) 241-245.

[10] H. Shokrollahi: *J. Magn. Mag. Mater.* **426** (2017) 74-81.

[11] C.A. Gorski, M.M. Scherer: *American Mineralogist* **95** (2010) 1017-1026.

[12] C.J. Goss: *Phys. Chem. Minerals* **16** (1988) 164-171.

[13] E.M. Gyorgy, H.M. O'Bryan Jr.: *Physics Letters* **23** (1966) 513-514.

[14] C.A. Gorski, M.M. Scherer: *Environ. Sci. Technol.* **43** (2009) 3675–3680.

[15] O.N. Shebanova, P. Lazor: *J. Solid State Chem.* **174** (2003) 424-430.

[16] T. Yamashita, P. Hayes: *Appl. Surface Sci.* **254** (2008) 2441-2449.

[17] I. Radisavljević, B. Kuzmanović,, N. Novaković, H.-E. Mahnke, L.J. Vulićević, S. Kurko, N. Ivanović: *Journal of Alloys and Compounds* **697** (2017) 409-416.

[18] R.E. Vandenberghe, C.A. Barrero, G.M. da Costa, E. Van San, E. De Grave: *Hyperfine Interactions* **126** (2000) 247-259.

[19] C.E. Johnson, J.A. Johnson, H.Y. Hah, M. Cole, S. Gray, V. Kolesnichenko, P. Kucheryavy, G. Goloverda: *Hyperfine Interact* **237** (2016) 27-36.

[20] A. Joos, C. Rümenapp, F.E. Wagner, B. Gleich: *J. Magn. Mag. Mater.* **399** (2016) 123-129.

[21] W.C. Hamilton: *Phys. Rev.* **110** (1958) 1050-1057.

[22] G.Kh. Rozenberg, M.P. Pasternak, W.M. Xu, Y. Amiel, M. Hanfland, M. Amboage, R.D. Taylor, R. Jeanloz: *Phys. Rev. Lett.* **96** (2006) 045705 1-4.

[23] D.B. Bonstrom, A.H. Morrish, L.A.K. Watt: *J. Appl. Phys.* **32** (1961) S272-S273.

[24] J.S. Salazar, L. Perez, O. de Abril, L.T. Phuoc, D. Ihiawakrim, M. Vazquez, J.M. Greneche, S. Begin-Colin, G. Pourroy: *Chem. Mater.* **23** (2011) 1379-1386.

[25] R. Aragón, D.J. Buttrey, J.P. Shepherd, J.M. Honig: *Phys. Rev. B* **31** (1984) 430-436.

[26] E. De Grave, R.M. Persoons, R.E. Vandenberghe, P.M.A. de Bakker: *Phys. Rev. B* **47** (1993) 5881-5893.

[27] A.W. Burton, K. Ong, T. Rea, I.Y. Chan: *Micropor. Mesopor. Mat.* **117** (2009) 75-90.

[28] Z. Klencsár, E. Kuzmann, A. Vértes: *J. Radioanal. Nucl. Chem.* **210** (1996) 105-118.

[29] Z. Klencsár: *Hyperfine Interactions* **217** (2013) 117-126.

[30] B.P. Weiss, S.S. Kim, J.L. Kirschvink, R.E. Kopp, M. Sankaran, A. Kobayashi, A. Komeili: *Earth and Planetary Science Letters* **224** (2004) 73-89.

[31] E. Schlömann: *J. Phys. Chem. Solids* **6** (1958) 257-266.

[32] R.S. de Biasi, T.C. Devezas: *J. Appl. Phys.* **49** (1978) 2466-2469.

[33] Q. Song, Z.J. Zhang: *J. Phys. Chem. B* **110** (2006) 11205-11209.

[34] Z. Homonnay, Gy. Tolnai, F. Fodor, A. Solti, K. Kovács, E. Kuzmann, A. Ábrahám, E.Gy. Szabó, P. Németh, L. Szabó, Z. Klencsár: *Hyperfine Interactions* **237** (2016) 127-135.

[35] J. Hesse, A. Rübartsch: *J. Phys. E: Sci. Instrum.* **7** (1974) 526-532.

[36] Z. Klencsár, Gy. Tolnai, L. Korecz, I. Sajó, P. Németh, J. Osán, S. Mészáros, E. Kuzmann: *Solid State Sciences* **24** (2013) 90-100.

Table 1. Room-temperature ^{57}Fe Mossbauer parameters of the prepared samples, derived on the basis of the fit model described in the text. δ stands for the ^{57}Fe isomer shift and W_L for the FWHM Lorentzian line width of the individual absorption peaks the models are composed from. The latter was assumed to be the same for the $Fe^{2.5+}$ and Fe^{3+} components, and furthermore for all of the samples. Isomer shifts of the Fe^{3+} components were assumed to be the same in all of the samples. The isomer shift of the $Fe^{2.5+}$ component is drawn as a function of the relative area fraction of the same component on Figure 9. Standard error (σ) in the last digit(s) of the quoted fit parameter values are given in parentheses. Concerning the relative area fraction and the isomer shift of the $Fe^{2.5+}$ component, σ was calculated by keeping all other fit parameters fixed.

Sample	**M1a**	**M1b**	**M2**	**M3a**	**M3b**	**M4**
$Fe^{2.5+}$ component						
Relative area fraction, %	26.8(0.9)	28.2(0.5)	22.5(1.0)	34.8(0.6)	29.9(0.5)	36.1(0.5)
δ, mm s^{-1}	0.569(18)	0.535(11)	0.562(23)	0.603(13)	0.581(11)	0.658(13)
W_L, mm s^{-1}	0.387(5)					
Fe^{3+} component						
Relative area fraction, %	73.2(1.2)	71.8(0.9)	77.5(1.3)	65.2(0.8)	70.1(0.8)	63.9(0.7)
δ, mm s^{-1}	0.295(3)					
W_L, mm s^{-1}	0.387(5)					

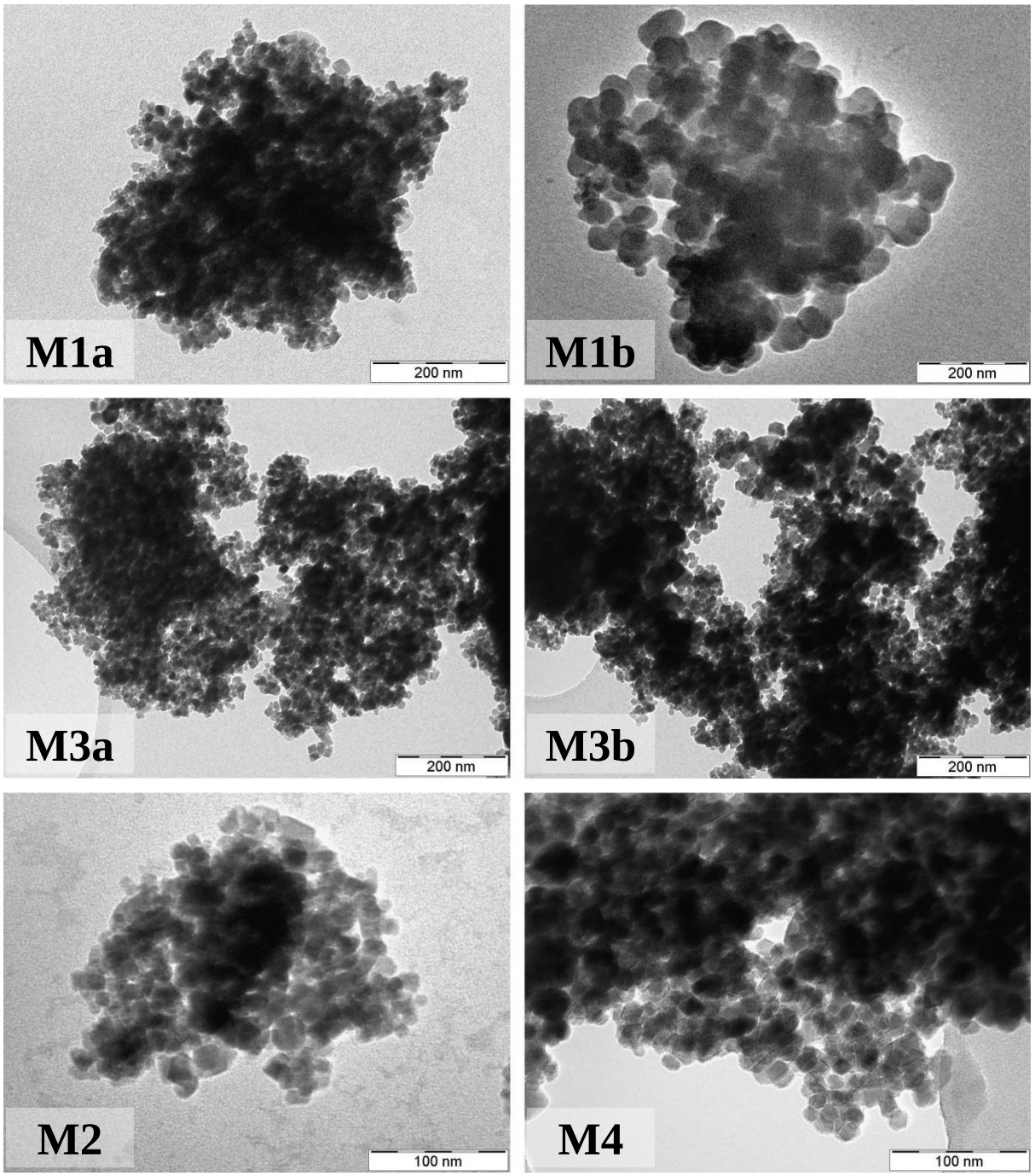

Figure 1. TEM images of the prepared powder samples. Note the different scale in the case of the samples M2 and M4.

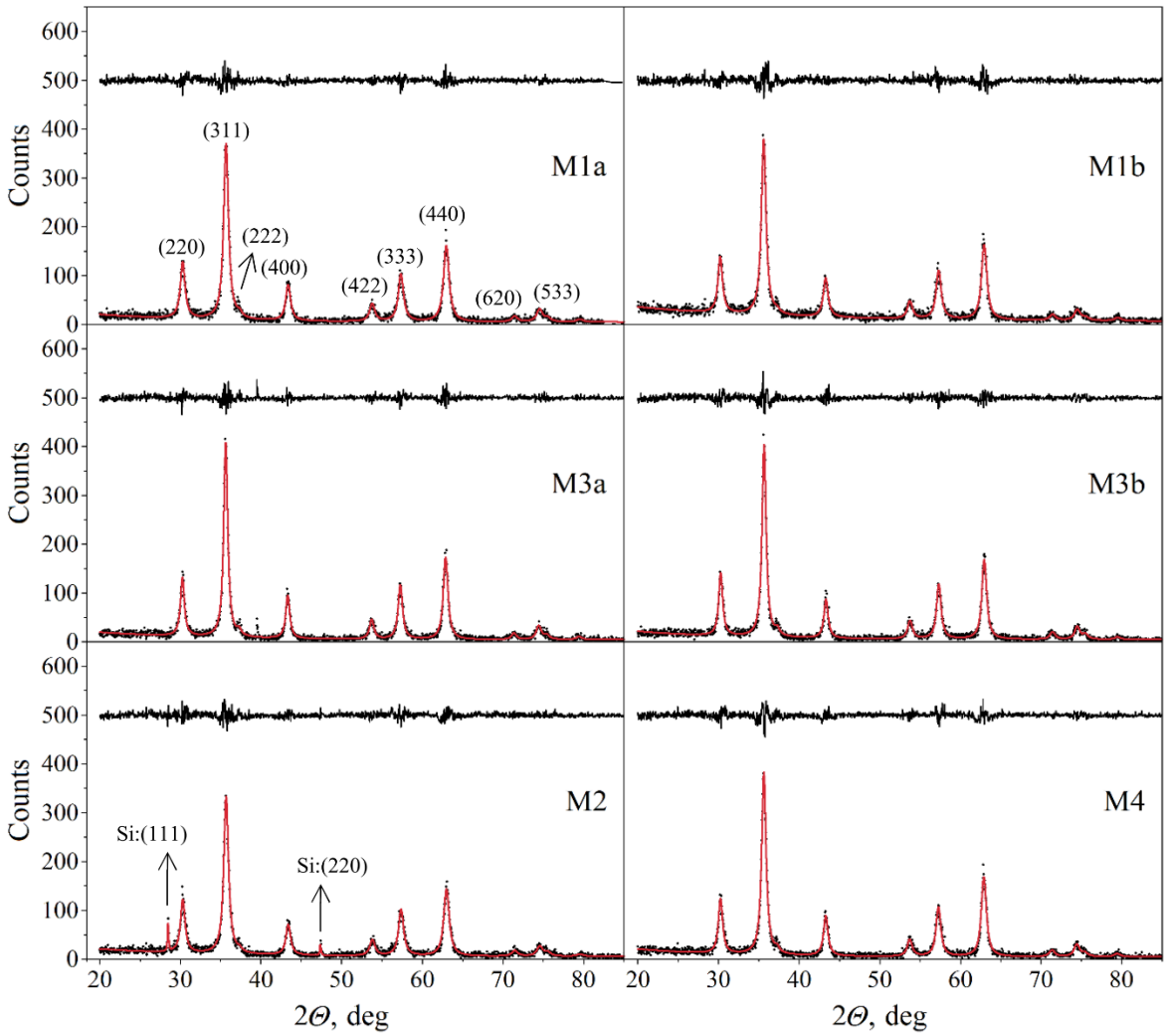

Figure 2. Powder X-ray diffractograms of the prepared samples (recorded with Cu K_α radiation) along with the corresponding fitting curves, with the cubic spinel (hkl) indexes indicated in the case of M1a. Silicon powder was mixed with sample M2 in order to calibrate the 2Θ axis. Above the diffractograms the respective fit residuals are displayed. The sharp peak at 2Θ = 39.5 deg, observed only for M3a, remained unidentified and is regarded as an artifact.

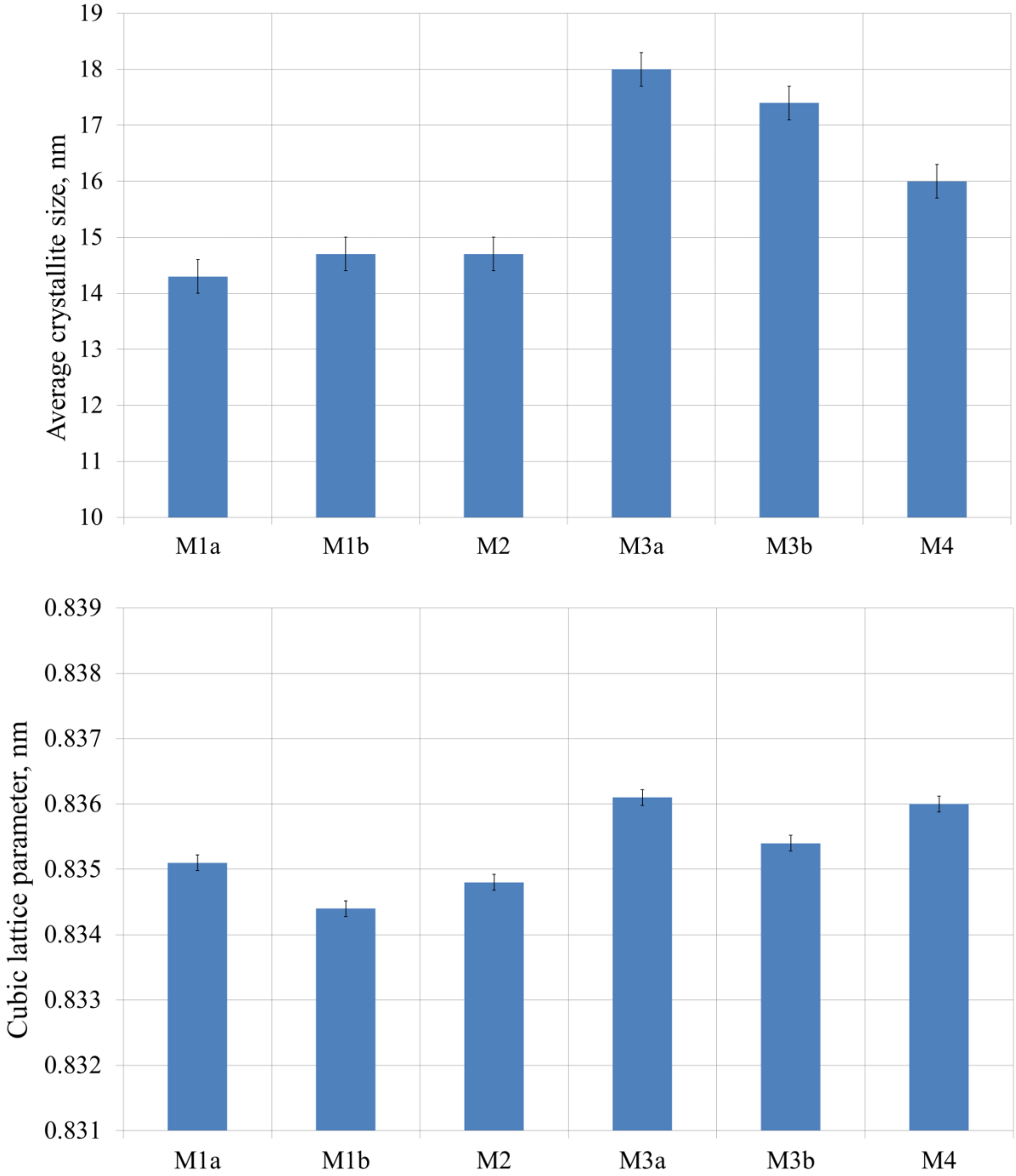

Figure 3. Average crystallite size (top) and cubic lattice parameter (bottom) derived on the basis of the powder X-ray diffractograms (Figure 2) of the prepared samples. Standard error (σ) of the crystallite size values is ~ 0.1 nm, and that of the lattice parameter values is ~ 4×10^{-5} nm. The error bars indicate ±3σ.

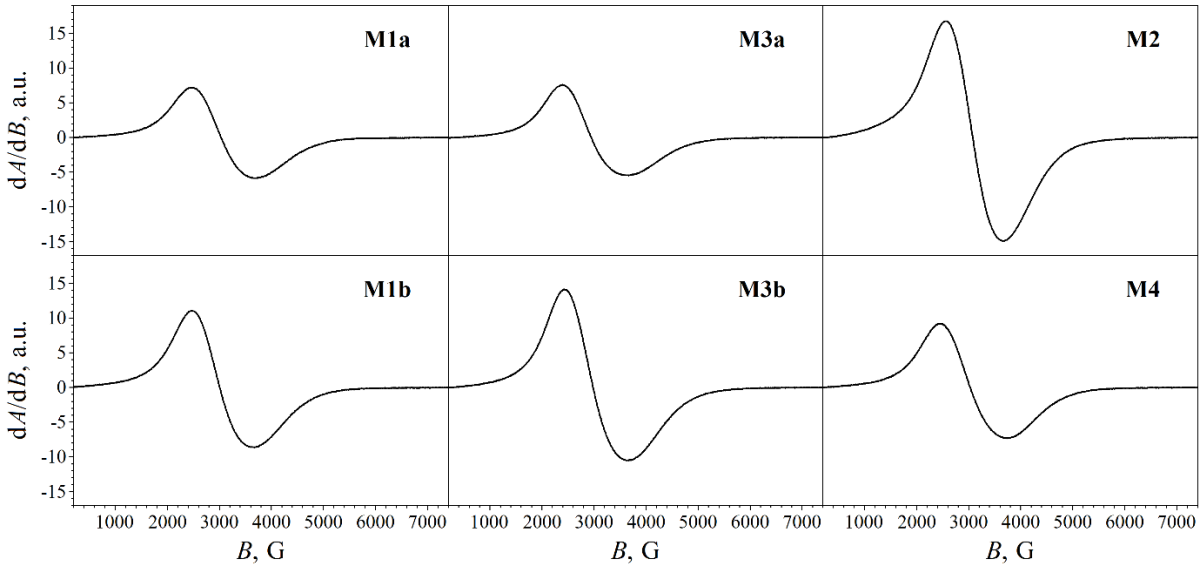

Figure 4. X-band electron magnetic resonance spectra of 0.1 mg of the powder samples evenly mixed with 19.9 mg KBr.

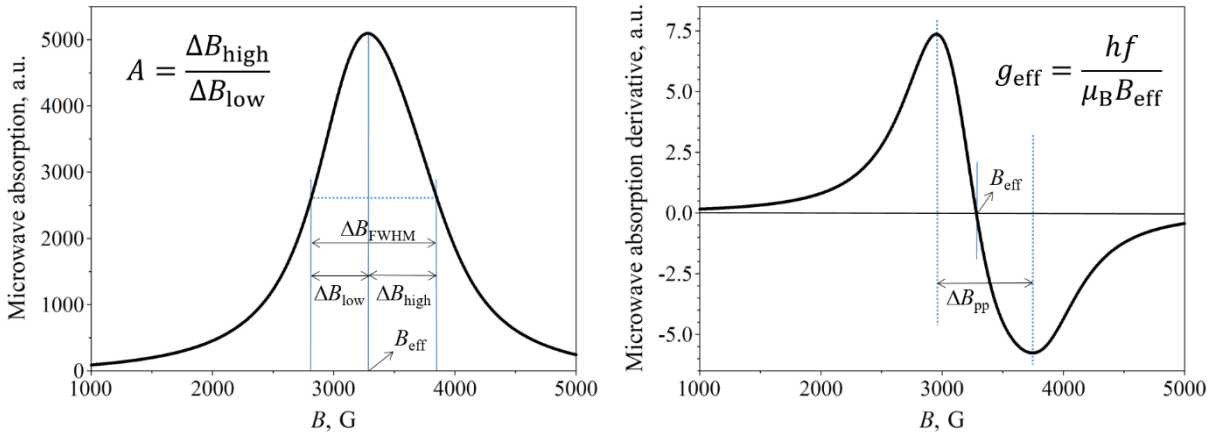

Figure 5. Definition of ferromagnetic resonance spectrum parameters *A* (asymmetry ratio) and g_{eff} : a hypothetical microwave absorption spectrum is shown on the left, whereas the corresponding absorption derivative spectrum is shown on the right. The index FWHM stands for 'full width at half maximum', pp stands for 'peak-to-peak', *h* is the Planck constant, and μ_{B} is the Bohr magneton.

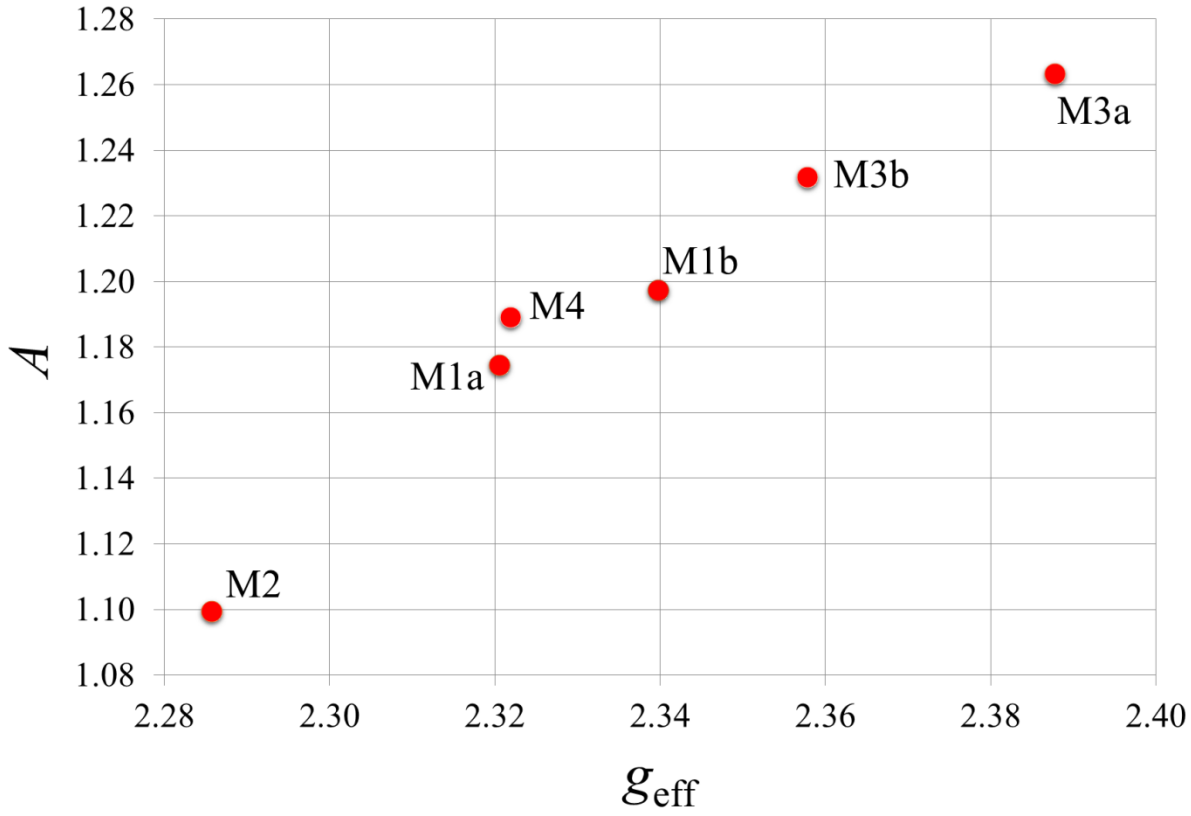

Figure 6. *A* (asymmetry ratio) depicted as a function of g_{eff} (Figure 6) for each of the prepared samples, as determined on the basis of the corresponding X-band electron magnetic resonance spectra (Figure 4). The uncertainty of the *A* values is below ~ 0.01, while that of the g_{eff} values is below ~ 0.002.

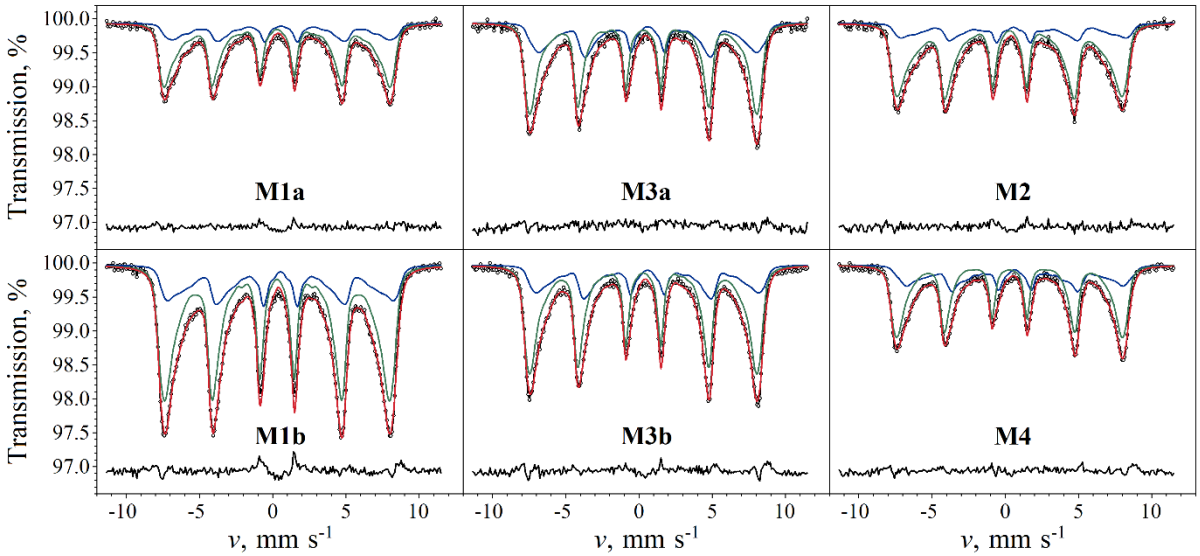

Figure 7. Room-temperature ^{57}Fe Mössbauer spectra (depicted with circles) of the prepared samples with the indication of the fit envelope (solid line through the circles) and the two subcomponents of the fit (solid lines). The fit residuals are displayed below the spectra.

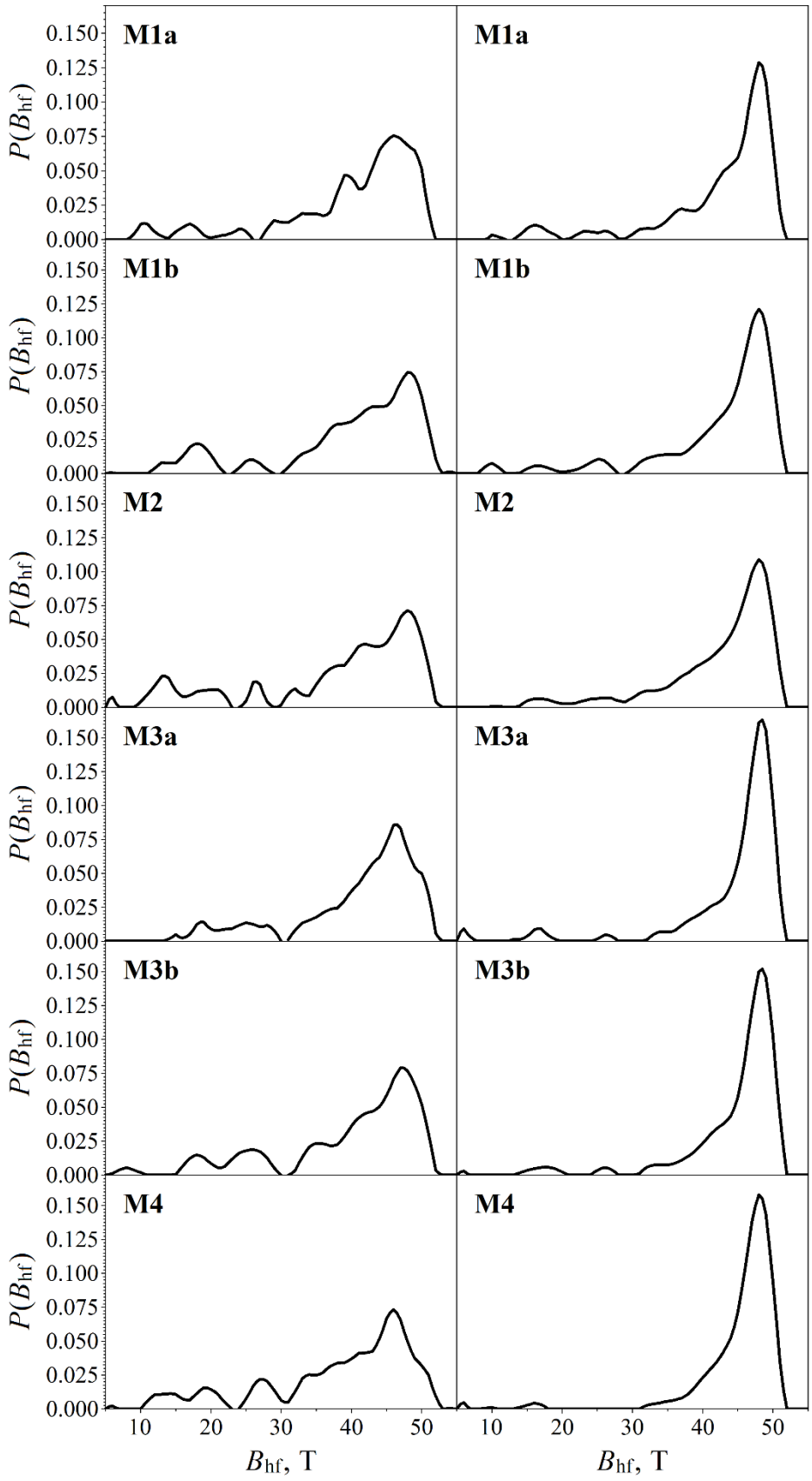

Figure 8. Hyperfine magnetic field distributions derived on the basis of the room-temperature ^{57}Fe Mössbauer spectra of the prepared samples (Figure 7). The left column shows distributions associated with the intermediate valence $Fe^{2.5+}$ component, whereas the right column displays distributions associated with Fe^{3+}.

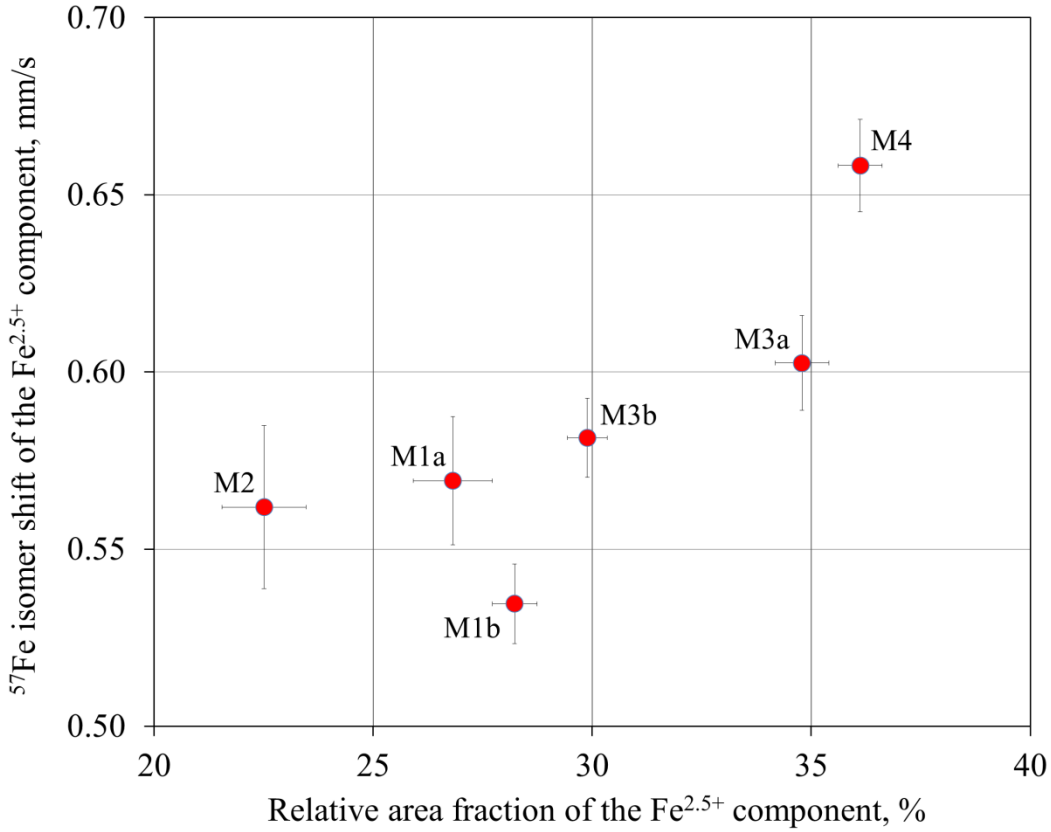

Figure 9. Room-temperature ^{57}Fe isomer shift associated with the intermediate-valence iron ions in the prepared samples depicted as a function of the Mössbauer spectrum area fraction of the corresponding broadened sextet subcomponent. Error bars refer to the standard error of the data.

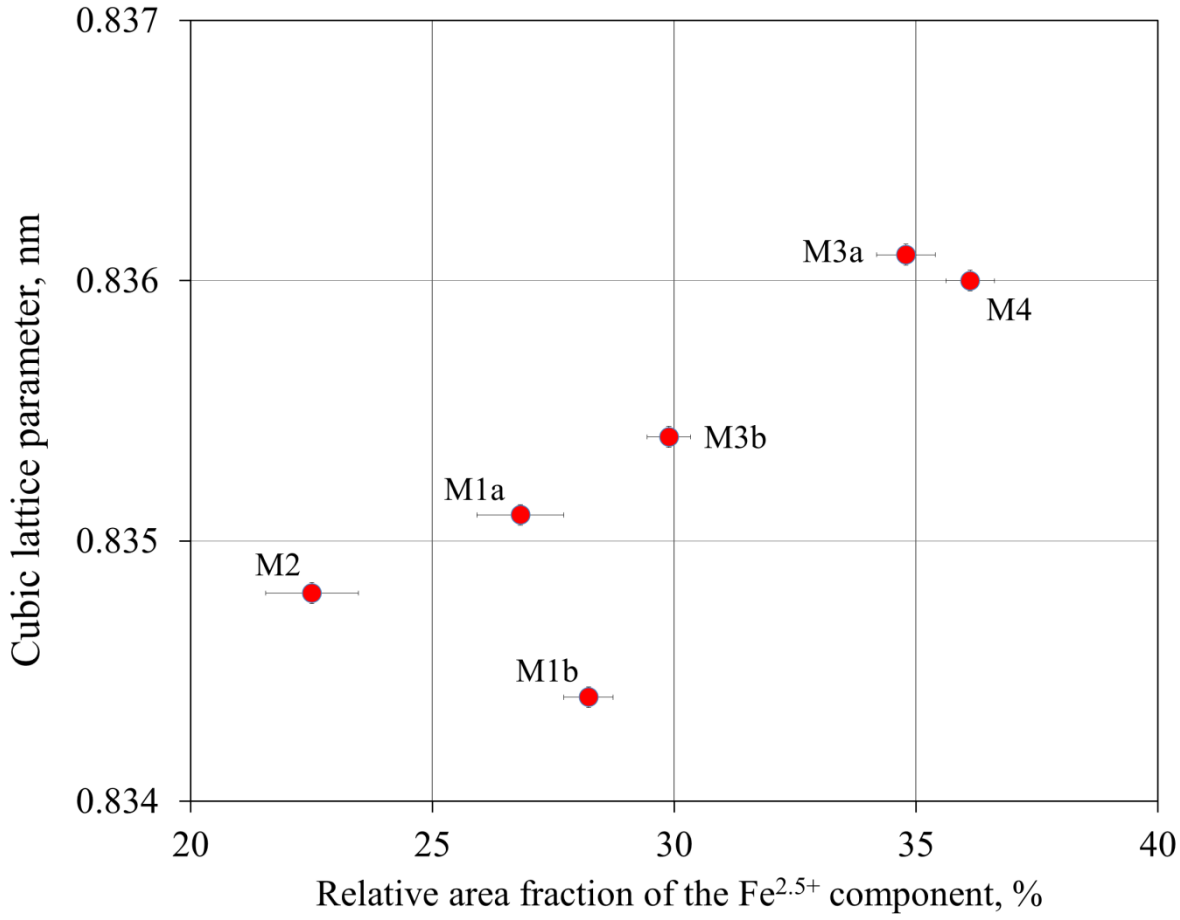

Figure 10. The cubic lattice parameter of the prepared samples depicted as a function of the relative area fraction of the $Fe^{2.5+}$ component as determined on the basis of room-temperature Mössbauer spectra (Figure 7). See Table 1 and Figure 3 for corresponding data. Error bars refer to the standard error of the data.

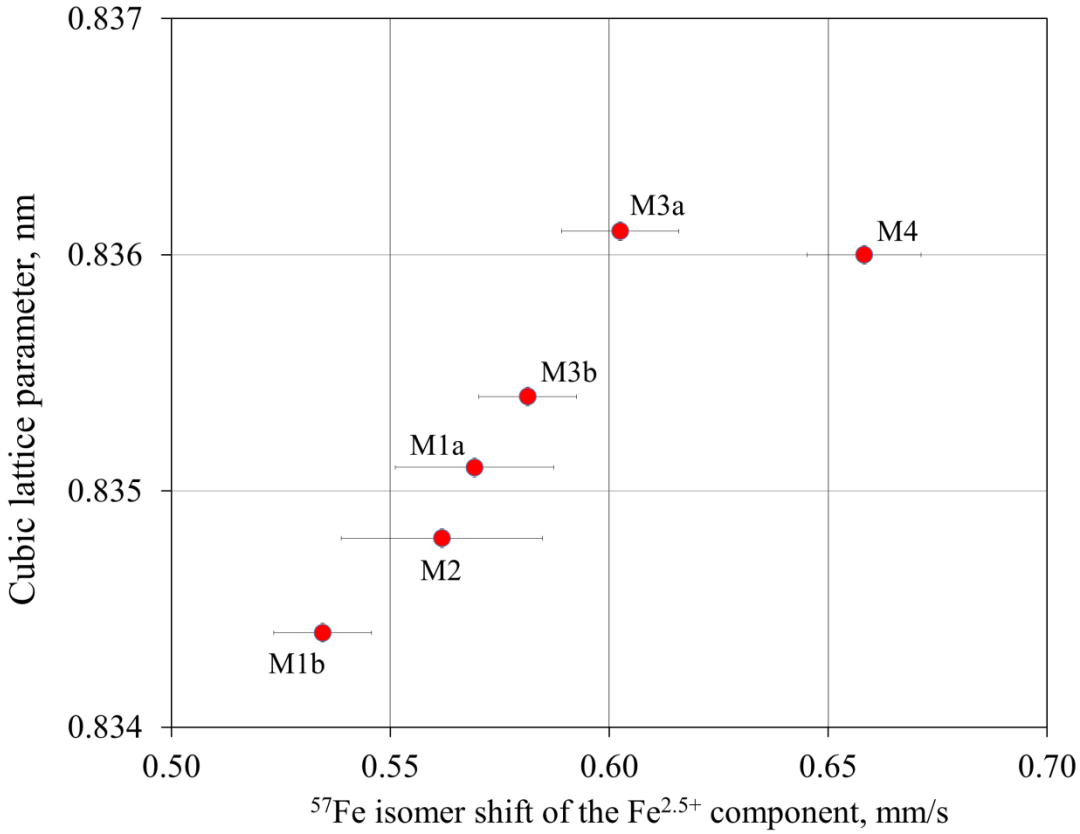

Figure 11. The cubic lattice parameter of the prepared samples depicted as a function of the ^{57}Fe isomer shift of the $Fe^{2.5+}$ component as determined on the basis of room-temperature Mössbauer spectra (Figure 7). See Table 1 and Figure 3 for corresponding data. Error bars refer to the standard error of the data.

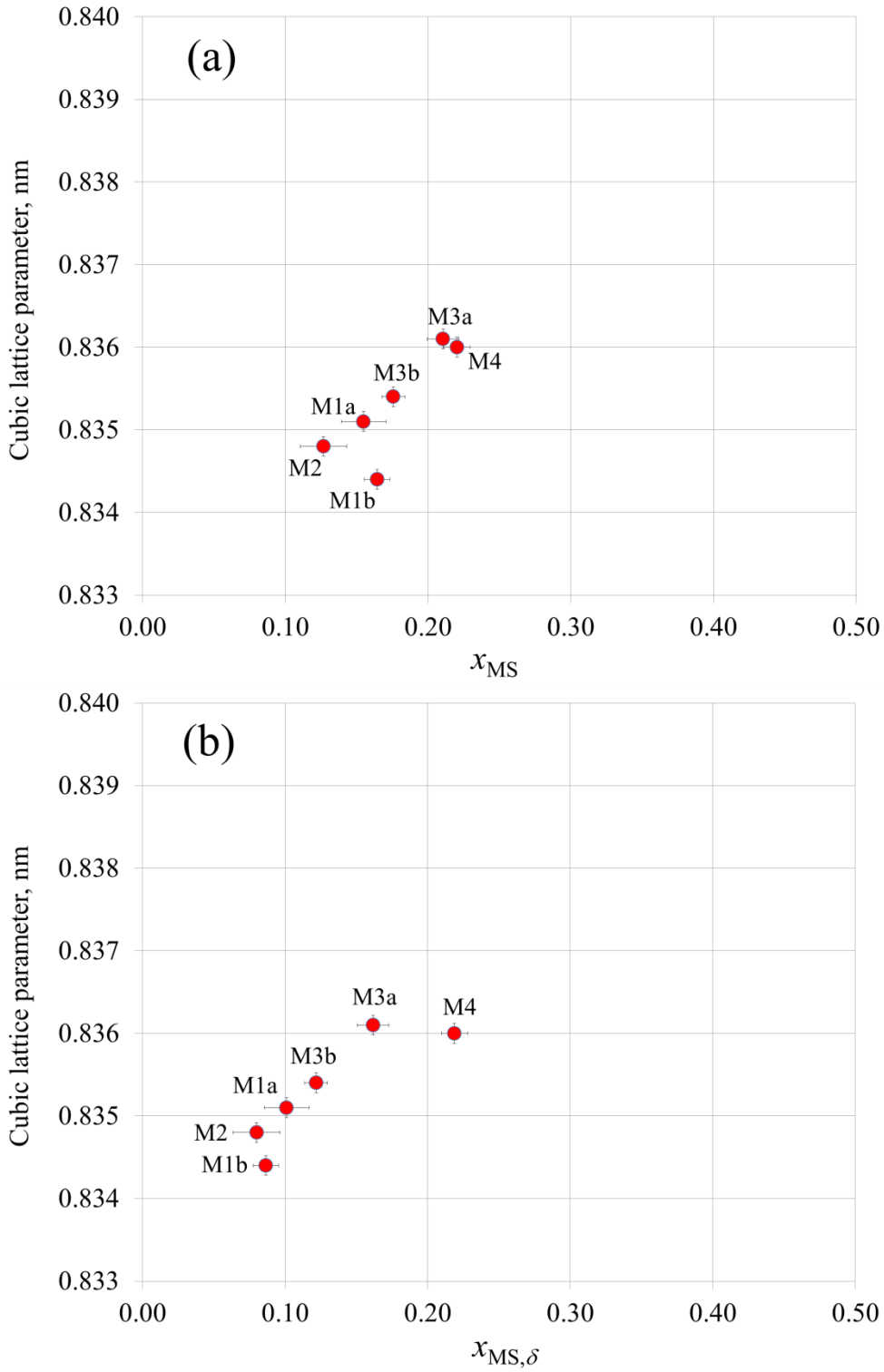

Figure 12. Dependence of the cubic lattice parameter on (a) the x_{MS} (see Eq. (2)) and (b) the $x_{MS,\delta}$ (see Eq. (3)) approximation of the hypothetical Fe^{2+}/Fe^{3+} ratio in the studied samples, as derived on the basis of the room-temperature ^{57}Fe Mössbauer spectra (Figure 7). The error bars reflect approximation of 3σ, where σ is the standard error.

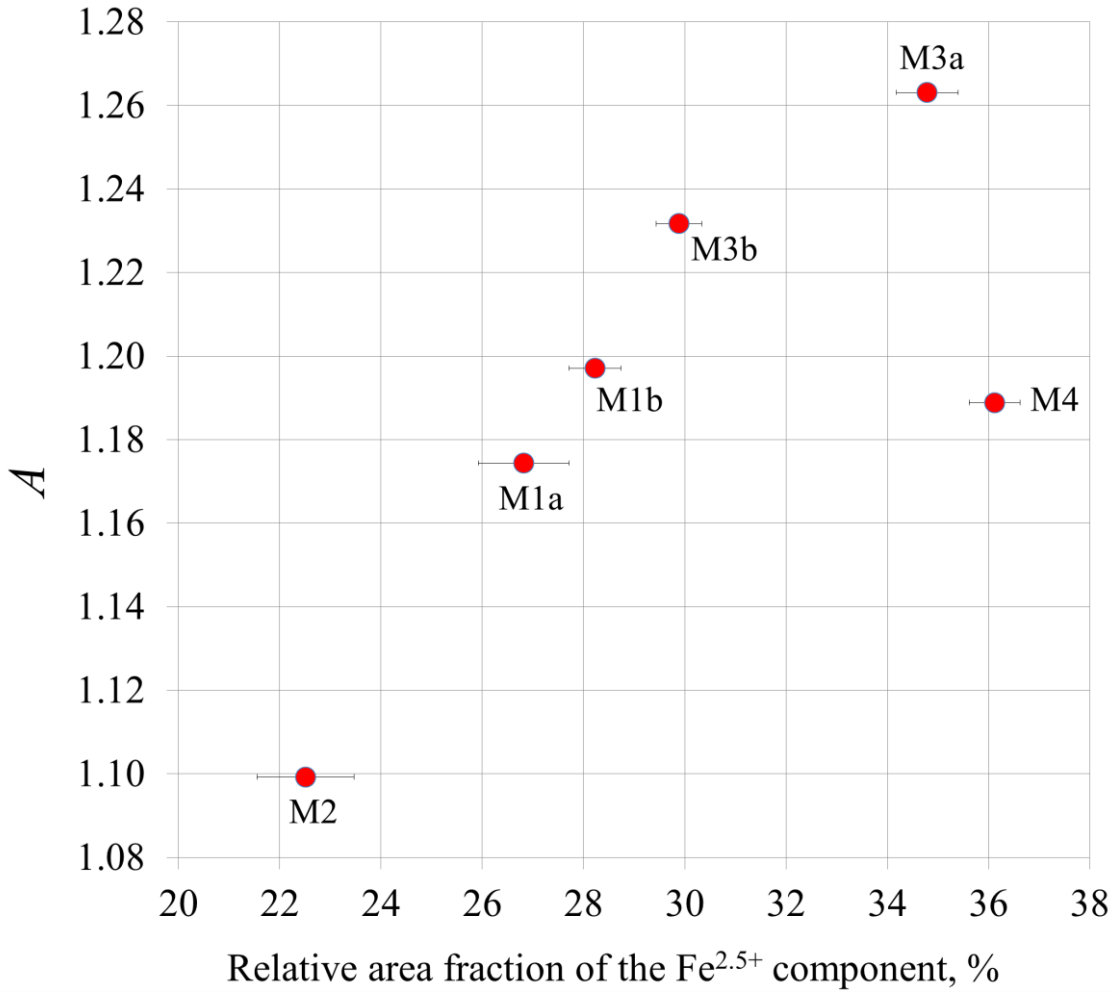

Figure 13. Asymmetry ratio *A* determined on the basis of EMR spectra shown in Figure 4, depicted as a function of the Mössbauer spectrum area fraction of the broadened sextet subcomponent associated with intermediate valence iron ions, as determined on the basis of the ^{57}Fe Mössbauer spectra shown in Figure 7. The uncertainty of the *A* values is below ~ 0.01.